

REPORT DOCUMENTATION PAGE				Form Approved OMB NO. 0704-0188	
<p>The public reporting burden for this collection of information is estimated to average 1 hour per response, including the time for reviewing instructions, searching existing data sources, gathering and maintaining the data needed, and completing and reviewing the collection of information. Send comments regarding this burden estimate or any other aspect of this collection of information, including suggestions for reducing this burden, to Washington Headquarters Services, Directorate for Information Operations and Reports, 1215 Jefferson Davis Highway, Suite 1204, Arlington VA, 22202-4302. Respondents should be aware that notwithstanding any other provision of law, no person shall be subject to any penalty for failing to comply with a collection of information if it does not display a currently valid OMB control number.</p> <p>PLEASE DO NOT RETURN YOUR FORM TO THE ABOVE ADDRESS.</p>					
1. REPORT DATE (DD-MM-YYYY) 04-01-2013		2. REPORT TYPE Final Report		3. DATES COVERED (From - To) 1-Nov-2008 - 31-Oct-2012	
4. TITLE AND SUBTITLE "Uncooled split-off quantum infrared sensors for 3-5 micron imaging applications"			5a. CONTRACT NUMBER W911NF-08-1-0448		
			5b. GRANT NUMBER		
			5c. PROGRAM ELEMENT NUMBER 611102		
6. AUTHORS A. G. Unil Perera, Y Lao			5d. PROJECT NUMBER		
			5e. TASK NUMBER		
			5f. WORK UNIT NUMBER		
7. PERFORMING ORGANIZATION NAMES AND ADDRESSES Georgia State University Office of Sponsored Programs Georgia State University Research Foundation, Inc. Atlanta, GA 30302 -3999				8. PERFORMING ORGANIZATION REPORT NUMBER	
9. SPONSORING/MONITORING AGENCY NAME(S) AND ADDRESS(ES) U.S. Army Research Office P.O. Box 12211 Research Triangle Park, NC 27709-2211				10. SPONSOR/MONITOR'S ACRONYM(S) ARO	
				11. SPONSOR/MONITOR'S REPORT NUMBER(S) 54109-EL.30	
12. DISTRIBUTION AVAILABILITY STATEMENT Approved for Public Release; Distribution Unlimited					
13. SUPPLEMENTARY NOTES The views, opinions and/or findings contained in this report are those of the author(s) and should not be construed as an official Department of the Army position, policy or decision, unless so designated by other documentation.					
14. ABSTRACT A detector concept utilizing hole transitions from the light-hole/heavy-hole (LH/HH) band to the spin-orbit split-off (SO) band has been developed to achieve room temperature operation. The p-type GaAs/Al _x Ga _{1-x} As multiple heterojunction detectors with the threshold wavelength of 4 μm demonstrated uncooled operation. Investigations further showed that response extension can be realized by including hole transitions between LH and HH bands. Spectral response up to 16.5 μm, operating up to a temperature of 330 K has been obtained, where the LH-HH					
15. SUBJECT TERMS Infrared Detectors, Room Temperature, Split off, graded Barrier, Intervalence Band (IVB) transitions					
16. SECURITY CLASSIFICATION OF:			17. LIMITATION OF ABSTRACT UU	15. NUMBER OF PAGES	19a. NAME OF RESPONSIBLE PERSON Unil Perera
a. REPORT UU	b. ABSTRACT UU	c. THIS PAGE UU			19b. TELEPHONE NUMBER 404-413-6037

Report Title

"Uncooled split-off quantum infrared sensors for 3-5 micron imaging applications"

ABSTRACT

A detector concept utilizing hole transitions from the light-hole/heavy-hole (LH/HH) band to the spin-orbit split-off (SO) band has been developed to achieve room temperature operation. The p-type GaAs/Al_xGa_{1-x}As multiple heterojunction detectors with the threshold wavelength of 4 μm demonstrated uncooled operation. Investigations further showed that response extension can be realized by including hole transitions between LH and HH bands. Spectral response up to 16.5 μm, operating up to a temperature of 330 K has been obtained, where the LH-HH response is superimposed on the free-carrier response. Analysis on the dark current mechanisms was carried out on these high-operating-temperature split-off detectors in order to improve electrical uniformity. Further optimization using graded barriers with an offset between the barriers on the two sides of an emitter was explored as a method of reducing the capture rate of photocarriers in the emitters. Experiments showed that responsivity increased by a factor of 10 or more was measured in graded-barrier detectors in comparison with detectors without the graded barrier. The graded barrier structure is also shown to be capable of operating in photovoltaic model and a good candidate for high-temperature photovoltaic detectors.

Enter List of papers submitted or published that acknowledge ARO support from the start of the project to the date of this printing. List the papers, including journal references, in the following categories:

(a) Papers published in peer-reviewed journals (N/A for none)

<u>Received</u>	<u>Paper</u>
-----------------	--------------

- | | |
|------------|--|
| 07/16/2012 | 1.00 Yan-Feng Lao, A. G. Unil Perera. Dielectric function model for p-type semiconductor inter-valence band transitions,
Journal of Applied Physics, (05 2011): 0. doi: 10.1063/1.3590138 |
| 07/16/2012 | 2.00 A. G. Unil Perera, M. S. Shishodia. Heterojunction plasmonic midinfrared detectors,
Journal of Applied Physics, (02 2011): 0. doi: 10.1063/1.3548896 |
| 07/16/2012 | 3.00 Y. F. Lao, P. K. D. D. P. Pitigala, A. G. U. Perera, H. C. Liu, M. Buchanan, Z. R. Wasilewski, K. K. Choi, P. Wijewarnasuriya. Light-hole and heavy-hole transitions for high-temperature long-wavelength infrared detection,
Applied Physics Letters, (09 2010): 0. doi: 10.1063/1.3486169 |
| 07/16/2012 | 4.00 A.G.U. Perera, S.G. Matsik, D.P. Pitigala, Y.F. Lao, S.P. Khanna, L.H. Li, E.H. Linfield, Z.R. Wasilewski, M. Buchanan, X.H. Wu, H.C. Liu. Effects of graded barriers on the operation of split-off band infrared detectors,
Infrared Physics & Technology, (05 2011): 0. doi: 10.1016/j.infrared.2010.12.033 |
| 07/16/2012 | 6.00 P. K. D. D. P. Pitigala, S. G. Matsik, A. G. U. Perera, S. P. Khanna, L. H. Li, E. H. Linfield, Z. R. Wasilewski, M. Buchanan, H. C. Liu. Photovoltaic infrared detection with p-type graded barrier heterostructures,
Journal of Applied Physics, (04 2012): 0. doi: 10.1063/1.4704695 |
| 07/16/2012 | 7.00 S. G. Matsik, P. V. V. Jayaweera, A. G. U. Perera, K. K. Choi, P. Wijewarnasuriya. Device modeling for split-off band detectors,
Journal of Applied Physics, (09 2009): 0. doi: 10.1063/1.3224873 |
| 07/16/2012 | 8.00 A.G.U. Perera, P.V.V. Jayaweera, S.G. Matsik, H.C. Liu, M. Buchanan, Z.R. Wasilewski. Operating temperature and the responsivity of split-off band detectors,
Infrared Physics & Technology, (11 2009): 0. doi: 10.1016/j.infrared.2009.05.024 |
| 07/16/2012 | 9.00 Y. F. Lao, P. V. V. Jayaweera, Steven G. Matsik, A. G. Unil Perera, H. C. Liu, M. Buchanan, Z. R. Wasilewski. Analysis of Dark Current Mechanisms for Split-Off Band Infrared Detectors at High Temperatures,
IEEE Transactions on Electron Devices, (06 2010): 0. doi: 10.1109/TED.2010.2046065 |
| 07/16/2012 | 10.00 P. Viraj Vishwakantha Jayaweera, P. K. D. Duleepa P. Pitigala, Jia Feng Shao, Kirthi Tennakone, A. G. Unil Perera, Pradeep M. Jayaweera, Jonas Baltusaitis. Low-Cost ZnO-Based Ultraviolet-Infrared Dual-Band Detector Sensitized With PbS Quantum Dots,
IEEE Transactions on Electron Devices, (10 2010): 0. doi: 10.1109/TED.2010.2059631 |
| 07/16/2012 | 11.00 M.S. Shishodia, P.V.V. Jayaweera, S.G. Matsik, A.G.U. Perera, H.C. Liu, M. Buchanan. Surface plasmon enhanced IR absorption: Design and experiment,
Photonics - Nanostructures - Fundamentals and Applications, (02 2011): 0. doi: 10.1016/j.photonics.2010.12.002 |
| 07/16/2012 | 12.00 P.K.D.D.P. Pitigala, P.V.V. Jayaweera, S.G. Matsik, A.G.U. Perera, H.C. Liu. Highly sensitive GaAs/AlGaAs heterojunction bolometer,
Sensors and Actuators A: Physical, (06 2011): 0. doi: 10.1016/j.sna.2011.02.017 |
| 07/16/2012 | 13.00 Yan-Feng Lao, Gamini Ariyawansa, A. G. Unil Perera. Design of resonant-cavity-enhanced multi-band photodetectors,
Journal of Applied Physics, (08 2011): 0. doi: 10.1063/1.3626812 |
| 07/16/2012 | 14.00 Subhananda Chakrabarti, Sourav Adhikary, Nilanjan Halder, Yigit Aytac, A. G. U. Perera. High-performance, long-wave (~10.2μm) InGaAs/GaAs quantum dot infrared photodetector with quaternary In _{0.21} Al _{0.21} Ga _{0.58} As capping,
Applied Physics Letters, (10 2011): 0. doi: 10.1063/1.3657142 |

TOTAL: 13

Number of Papers published in peer-reviewed journals:

(b) Papers published in non-peer-reviewed journals (N/A for none)

Received Paper

TOTAL:

Number of Papers published in non peer-reviewed journals:

(c) Presentations

“Graded-barrier heterostructures for photovoltaic split-off infrared detection”, IEEE Photonics 2012 (IPC12), Burlingame, California, September 23 - 27, 2012.

Number of Presentations: 1.00

Non Peer-Reviewed Conference Proceeding publications (other than abstracts):

Received Paper

TOTAL:

Number of Non Peer-Reviewed Conference Proceeding publications (other than abstracts):

Peer-Reviewed Conference Proceeding publications (other than abstracts):

<u>Received</u>	<u>Paper</u>
-----------------	--------------

07/16/2012	5.00	H. C. Liu, S. G. Matsik, D. P. Pitigala, A. G. U. Perera, Y. F. Lao, S. P. Khanna, L. H. Li, E. H. Linfield, Z. R. Wasilewski, M. Buchanan, X. H. Wu. Room temperature photovoltaic response of split-off band infrared detectors with a graded barrier, Quantum Sensing and Nanophotonic Devices VIII. 2010/01/24 00:00:00, San Francisco, California, USA. : ,
07/16/2012	21.00	S. G. Matsik, M. S. Shishodia, A. G. U. Perera, R. C. Jayasinghe, P. K. D. D. P. Pitigala. Spin split-off band-based high operating temperature IR detectors in 3-5 m and beyond, Infrared Technology and Applications XXXVI. 2010/04/05 00:00:00, Orlando, Florida, USA. : ,
07/16/2012	16.00	K. Tennakone, A. G. U. Perera, P. K. D. D. P. Pitigala. Performance enhancements of dye sensitized nanostructured solar cells using PbS quantum dots, Energy Harvesting and Storage: Materials, Devices, and Applications. 2010/04/05 00:00:00, Orlando, Florida, USA. : ,
07/16/2012	15.00	S. G. Matsik, M. S. Shishodia, R. C. Jayasinghe, A. G. Unil Perera. GaAs and GaN based high operating temperature spin split-off band infrared detectors, Quantum Sensing and Nanophotonic Devices VII. 2010/01/24 00:00:00, San Francisco, California, USA. : ,
07/20/2012	26.00	A. G. U. Perera, P. V. V. Jayaweera, S. G. Matsik. THz sensors based on spin orbit split off levels, 2009 34th International Conference on Infrared, Millimeter, and Terahertz Waves (IORMMW-THz 2009). 2009/09/21 00:00:00, Busan, South Korea. : ,

TOTAL: 5

Number of Peer-Reviewed Conference Proceeding publications (other than abstracts):

(d) Manuscripts

<u>Received</u>	<u>Paper</u>
-----------------	--------------

TOTAL:

Number of Manuscripts:

Books

Received

Paper

07/20/2012 25.00 A. G. U. Perera. a chapter titled "Homo and Hetero Junction Interfacial Work-Function Internal Photo-Emission Detectors from UV to IR" in the book "Advances in Infrared Photodetectors (Semiconductors and Semimetal Series)" edited by S. D. Gunapala, D.R. Rhiger, and C. Jagadish, New York: Elsevier Limited (ISBN: 978-0-12-381337-4), (01 2011)

TOTAL: 1

Patents Submitted

Patents Awarded

Awards

Regents' Professor - A.G. Unil Perera , 2012 October

IEEE Fellow, A. G. U. perera, 2012

Alumni Distinguished Professor- A. G. Unil Perera 2010

SPIE Fellow, A. G. Unil Perera, 2010

Graduate Students

<u>NAME</u>	<u>PERCENT SUPPORTED</u>	Discipline
Duleepa Pitigala	0.50	
Venkata Chargani	0.50	
Justin McLaughlin	0.25	
Hiren Patel	0.30	
FTE Equivalent:	1.55	
Total Number:	4	

Names of Post Doctorates

<u>NAME</u>	<u>PERCENT SUPPORTED</u>
Yan Lao	0.60
FTE Equivalent:	0.60
Total Number:	1

Names of Faculty Supported

<u>NAME</u>	<u>PERCENT SUPPORTED</u>	National Academy Member
A. G. U. Perera	0.09	
FTE Equivalent:	0.09	
Total Number:	1	

Names of Under Graduate students supported

<u>NAME</u>	<u>PERCENT SUPPORTED</u>	Discipline
Jennifer Rehm	0.50	Physics
FTE Equivalent:	0.50	
Total Number:	1	

Student Metrics

This section only applies to graduating undergraduates supported by this agreement in this reporting period

The number of undergraduates funded by this agreement who graduated during this period:	1.00
The number of undergraduates funded by this agreement who graduated during this period with a degree in science, mathematics, engineering, or technology fields:.....	1.00
The number of undergraduates funded by your agreement who graduated during this period and will continue to pursue a graduate or Ph.D. degree in science, mathematics, engineering, or technology fields:.....	1.00
Number of graduating undergraduates who achieved a 3.5 GPA to 4.0 (4.0 max scale):.....	1.00
Number of graduating undergraduates funded by a DoD funded Center of Excellence grant for Education, Research and Engineering:.....	0.00
The number of undergraduates funded by your agreement who graduated during this period and intend to work for the Department of Defense	0.00
The number of undergraduates funded by your agreement who graduated during this period and will receive scholarships or fellowships for further studies in science, mathematics, engineering or technology fields:	1.00

Names of Personnel receiving masters degrees

<u>NAME</u>
Duleepa Pitigala
Ranga Jayasinghe
Total Number:

2

Names of personnel receiving PHDs

<u>NAME</u>
Ranga Jayasinghe
Viraj Jayaweera
Total Number:

2

Names of other research staff

<u>NAME</u>	<u>PERCENT SUPPORTED</u>
FTE Equivalent:	
Total Number:	

Sub Contractors (DD882)

Inventions (DD882)

Scientific Progress

See Attachment

Technology Transfer

Uncooled Split Off Quantum Infrared Detectors for 3-5 micron Imaging Applications

Prepared by:

Dr. A. G. U. Perera and Dr. Yanfeng Lao

Georgia State University

Atlanta, GA 30303

FINAL REPORT

Project Period: 1st November 2008 – 31th October 2012

20th December 2012

Table of Contents

<u>Sections</u>	<u>Page</u>
1 Summary.....	1
2 Dector modeling and design.....	1
2.1 Device modeling for split-off band detectors	1
2.2 Analysis of Dark Current Mechanisms for Split-Off Band Infrared Detectors at High Temperatures.....	3
2.3 Design of resonant-cavity-enhanced photodetectors	5
3 Material characterization for detector design.....	7
3.1 Dielectric function model for <i>p</i> -type semiconductor inter-valence band transitions.....	7
3.2 Plasma frequency and dielectric function dependence on doping and temperature for p- type Indium Phosphide epitaxial films	8
3.3 Optical properties of nanostructured TiO ₂ thin films and their application as antireflection coatings on infrared detectors	10
4 Device results and discussion	11
4.1 Effects of Graded Barriers on the Operation of Split-Off Band Infrared Detectors	11
4.2 Split-off photovoltaic infrared detection with p-type graded barrier heterostructures ⁷	12
4.3 Light-hole and heavy-hole transitions for high-temperature long-wavelength infrared detection ⁹	15
4.4 ZnO-Based UltravioletInfrared Dual-Band Detector Sensitized With PbS Quantum Dots ¹⁰	16
4.5 Surface Plasmon for Optimizing Detector Performance ¹¹⁻¹² Heterojunction plasmonic midinfrared detectors	17
4.6 Highly sensitive GaAs/AlGaAs heterojunction bolometer ¹³	17
4.7 High-performance, long-wave (~ 10.2 μm) InGaAs/GaAs quantum dot infrared photodetector with quaternary In _{0.21} Al _{0.21} Ga _{0.58} As capping ¹⁴	18

1 SUMMARY

This final report describes the completed project “Uncooled Split Off Quantum Infrared Detectors for 3-5 micron Imaging Applications” with Proposal Number: 54109-EL and Agreement Number: W911NF-08-1-0448. The goal of the proposed research was to develop uncooled detectors. A detector concept, utilizing hole transitions from the light-hole/heavy-hole (LH/HH) band to the spin-orbit split-off (SO) band was developed to achieve room temperature operation. Investigations further showed that response extension can be realized by including hole transitions between LH and HH bands. A model based on the split-off transitions was developed for designing devices. Analysis on the dark current mechanisms was carried out on these high-operating-temperature split-off detectors in order to improve electrical uniformity. Further optimization using graded barriers with an offset between the barriers on the two sides of an emitter was explored as a method of reducing the capture rate of photocarriers in the emitters. The graded barrier structure is also shown to be capable of operating in photovoltaic mode and a good candidate for high-temperature photovoltaic detectors.

2 DETECTOR MODELING AND DESIGN

2.1 Device modeling for split-off band detectors

The approach to develop room temperature detectors use transitions between the light/heavy hole (LH/HH) bands and the spin-orbit split-off (SO) hole band to produce enhanced response at high temperature. Experimental results show that the devices can be designed for optimum operating temperature or optimum detectivity. A model was developed to calculate the dark and illuminated currents from the photoabsorption, carrier escape, and transport, explaining the experimental response. The variation of dark current, responsivity and detectivity with the detector parameters is investigated.¹

The split-off band detector response model consists of five parts: (i) calculation of absorption in the emitters including direct and indirect hole transitions from the LH/HH band to the SO band, (ii) calculation of excited carrier transport to the emitter/barrier interface, (iii) calculation of escape probability at the emitter/barrier interface, (iv) calculation of capture rate for injected carriers in the emitters, and (v) calculation of the dark and photocurrents.

This model was tested by comparing the calculated results with experimental measurements for three samples having free-carrier thresholds wavelength of 4, 6, and 8 μm . A reasonable agreement with the predicted peak response, i.e. within $\sim 20\%$ of the measured value for all the biases, as seen in

Figure 1, for the sample with a 4 μm threshold was achieved. The results for the 6 and 8 μm threshold samples were similar. The deviation seen at long wavelengths beyond $\sim 3.5 \mu\text{m}$ appears to be due to a thermal detection mode that is also present, which is not included in the modeling.

Using the carrier-carrier scattering lengths obtained from the fitting above, the effects of varying design parameters were investigated. For the calculations, the device structure consisted from

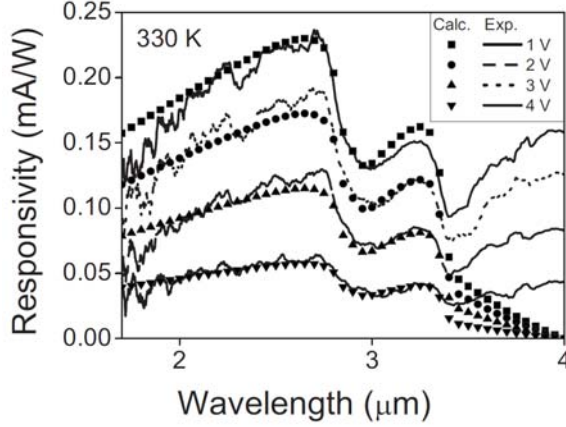


Figure 1: (a) The experimental spectra and the calculated response using the model for a sample having a 4 μm free-carrier threshold. There is good agreement except at the longer wavelengths. The disagreement at long wavelengths is due to the thermal mechanism which is not included in the model.

bottom to top of a GaAs bottom contact of thickness w_c with p -doping n_c , an undoped AlGaAs barrier layer of thickness w_b and Al fraction x_b , a p -doped GaAs emitter of thickness w_e and doping n_e , a top AlGaAs barrier with thickness w_t and Al fractions x_{t1} and x_{t2} at the bottom of the barrier, respectively, and a GaAs top contact of thickness w_c with p -doping n_c . By using different values for x_{t1} and x_{t2} , it is possible to include a graded barrier in the designs. For all calculations, the contact parameters were $w_c = 0.1 \mu\text{m}$ and $n_c = 1 \times 10^{19} \text{cm}^{-3}$. Figure 2 shows three detectors with different Al fractions. By varying the free-carrier threshold, it is possible to select the optimum combination of responsivity, D^* , and operating temperature for a specific application.

The effects of varying the emitter thickness on the response and the detectivity with $n_e = 3 \times 10^{18} \text{cm}^{-3}$ for detectors with 4, 6, and 8 μm free-carrier thresholds are shown in Figure 3. The

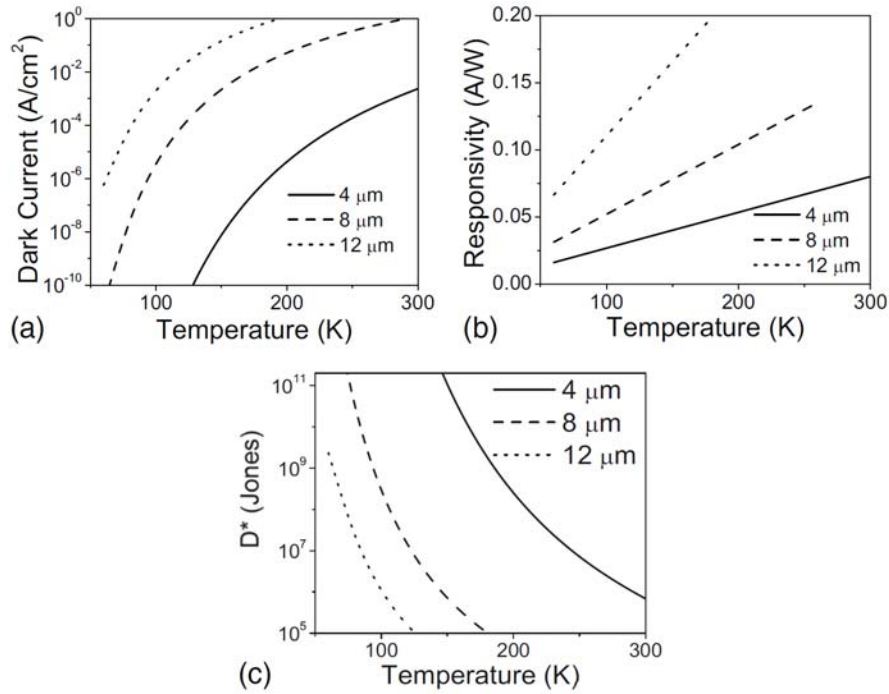


Figure 2: (a) The dark current, (b) responsivity, and (c) detectivity for detectors with free-carrier thresholds of 4, 8, and 12 μm at different temperatures at a bias of 1.0 V. The fixed detector parameters were $w_e = 20 \text{ nm}$, $n_e = 3 \times 10^{18} \text{cm}^{-3}$, $w_t = 50 \text{ nm}$, and $w_b = 1000 \text{ nm}$.

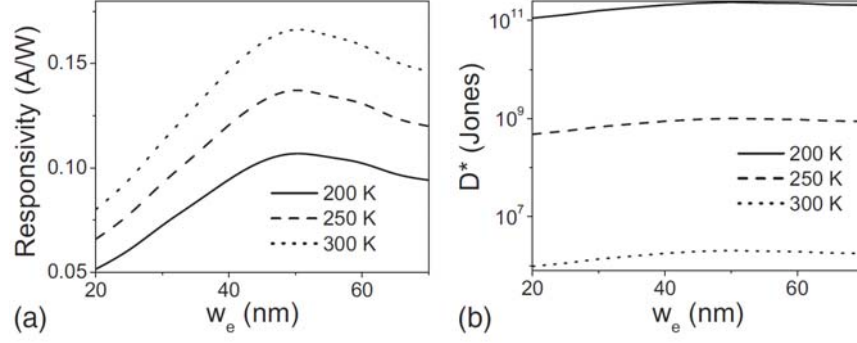


Figure 3: (a) The responsivity and (b) detectivity variation with emitter width for a detector with a free-carrier threshold of $4 \mu\text{m}$ at three different temperatures at a bias of 1.0 V. The fixed detector parameters were $n_e = 3 \times 10^{18} \text{ cm}^{-3}$, $w_t = 50 \text{ nm}$, and $w_b = 1000 \text{ nm}$.

response increased as the emitter thickness increased up to a value of $\sim 50 \text{ nm}$ due to the increasing absorption. For thicker emitters, the escape probability started to decrease, leading to a reduced response for emitters thicker than 50 nm .

In order to reduce the trapping and hence increase the gain, grading the top barrier in order to produce an offset between the barriers on the two sides of the emitter was explored. When the barrier on the injection side of the emitter is higher than that on the escape side, it will artificially heat the carriers entering the emitter. If the difference in heights is sufficiently large, the carriers will still be able to escape after scattering and the trapping rate will be greatly reduced. The increase in response with the difference in barrier height is shown in Figure 4. In designing detectors, the fact that gain applies to both the dark and photocurrents will need to be considered to determine the optimum value. The results indicate that increasing the gain above ~ 3 will not lead to any increase in D^* even though the response increases.

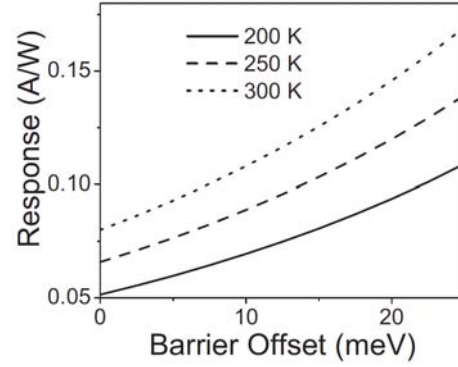


Figure 4: The responsivity variation with barrier offset for a detector with free-carrier threshold of $4 \mu\text{m}$ at three different temperatures at a bias of 1.0V. The fixed detector parameters were $w_e = 20 \text{ nm}$, $n_e = 3 \times 10^{18} \text{ cm}^{-3}$, $w_t = 50 \text{ nm}$, and $w_b = 1000 \text{ nm}$.

2.2 Analysis of Dark Current Mechanisms for Split-Off Band Infrared Detectors at High Temperatures

A model² including the two-dimensional (2D) transport characteristic of carriers was developed. Current-voltage-temperature (I-V-T) measurements on split-off detectors show that R_0A (product of zero-bias differential resistance and detector active area) deviation only occurs at high temperatures, indicating a temperature-dependent behavior of the electrical uniformity. A critical parameter, i.e., threshold temperature, defined by both experimental and theoretical results, represents the beginning of nonuniformity and needs to be optimized. Figure 5 (a) shows plots of

$\text{Log}[R_0A]$ versus $1000/T$ as measured on three detectors. The R_0A - T curve can be well fitted by the thermionic currents at the low-temperature end. However, when the temperature is increased,

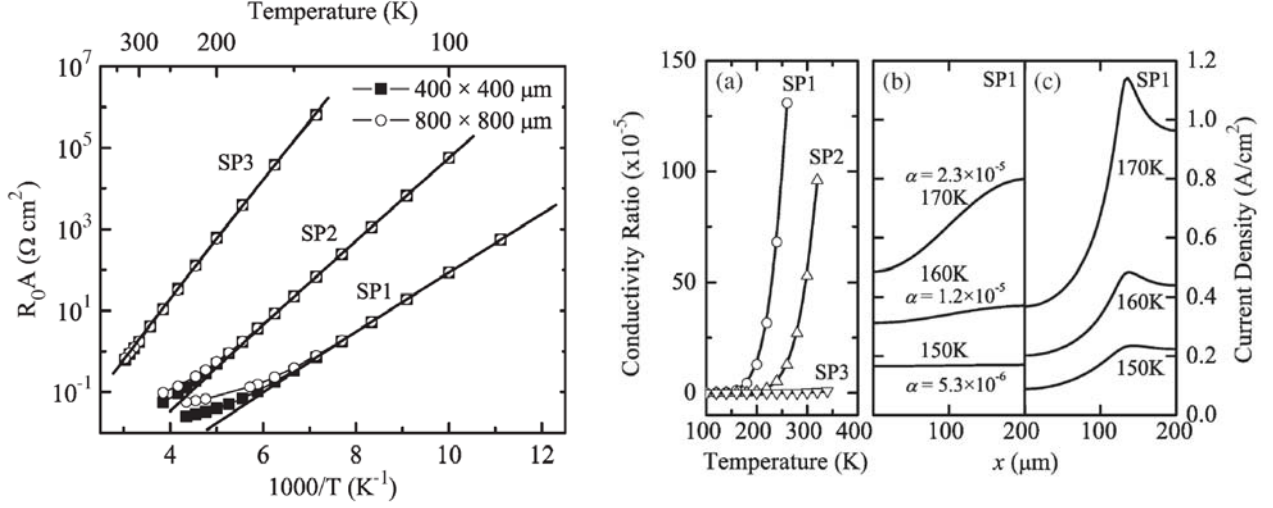


Figure 5: (a) Temperature-dependent R_0A for three detectors. The solid square and hollow circle data are for square-mesa devices with sizes of 400 and 800 μm , respectively. A fit to the low-temperature region (solid line) based on thermionic currents is extended to compare R_0A deviation at high temperatures. (a) Relation of calculated conductivity ratio (α) with temperatures for all devices. (b) and (c) are calculated lateral current distributions for the device SP1 with the mesa 400 $\mu\text{m} \times 400 \mu\text{m}$ at the interface between the active region and bottom contact layer, and the interface between top contact layer and active region, respectively. $x = 0$ represents the device center. The nonuniformity becomes remarkable when the temperature is increased.

R_0A starts to increase over the fitted value. This phenomenon is more prominent for devices with larger mesa sizes than that with smaller sizes.

The current nonuniformity originally results from the electric potential gradient in the lateral direction and depends on the conductivity ratio (α) of the vertical conductivity over the lateral conductivity. Figure 5(a) shows the calculated α - T relationship for three samples. Exponential increasing of α for SP1 takes place above 150 K, while SP3 has the same α with values close to zero over the entire temperature region up to 330 K. The vertical current for the sample SP1 is calculated as a function of lateral position x and is shown in Figure 5 (b) and (c).

Based on the theoretical model in Section III, two optimizations can be followed by either decreasing the vertical conductivity or increasing the lateral conductivity, both of which will reduce the conductivity ratio. Increasing the barrier height can efficiently increase the electrical uniformity of devices. However, changing barrier height also shifts the threshold wavelength of detectors and should be considered in the overall optimization. The lateral conductivity can be increased by decreasing barrier thickness or increasing emitter thickness and doping. Increasing emitter doping will also increase the absorption and thus responsivity.

2.3 Design of resonant-cavity-enhanced photodetectors

An investigation on the enhancement of quantum efficiency (QE) by resonant cavity was carried out.³ This method can improve QE of the region where absorption is low. For example, a multiple structure has an exponential degrading profile of light intensity from top to bottom. Enhancing optical field in the bottom region will benefit the overall improvement of QE. This cavity effect is demonstrated by employing a structure showing in Figure 6, consisting of different absorbing regions. Regions I, II, III, and IV can respond in VIS-NIR, MWIR, LWIR, and SWIR, respectively, by virtue of the optical processes due to inter-band transitions in the i-InP, inter-subband transitions in p-InGaAs/InP QWs, and the inter-band transitions in i-InGaAs.

To fabricate a Fabry-Perot (F-P) cavity, appropriate reflectors should be applied. A Bragg reflector normally becomes too thick in order to attain the high reflection in the LWIR. On the contrary, a Au film is capable of acting as a good reflector over the whole spectral range, e.g., a reflectivity of 98% for the InP-Au configuration, and is thus adopted as the bottom reflector. The top reflector can be the native InP-air interface which has the reflectivity varied from 27% at 1.5 μm to 17% at 12 μm .

The locations of the resonance modes are primarily determined by the cavity to which the optimizing was made. The reflection spectra are shown in Figure 7 (a) and (b). In the LWIR region, only one mode lies in the detection range of interest. Thus, the cavity should be properly adjusted. The optimization should also be able to maximize the overlapping between the optical field and the absorbing elements. With such considerations in mind, Figure 7 (c) plots the absorption enhancement factor for three detection bands. The maximum enhancement for region IV (SWIR), II (MWIR), and III (LWIR) is reached at the factors of 10.5, 9.5, and 11, respectively.

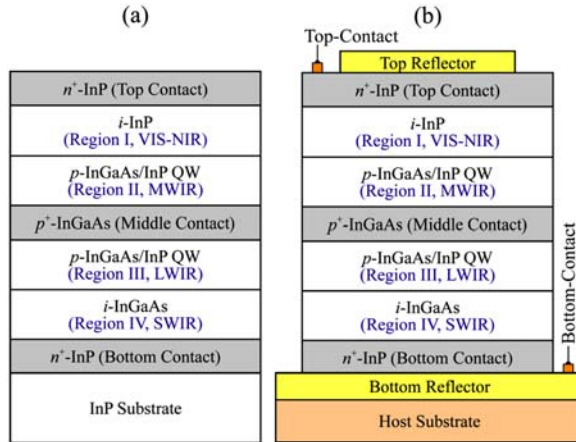


Figure 6: (a) A schematic of the conventional multi-band detector without the cavity. Regions I - IV correspond to four absorbing elements responding to different wavelengths. (b) The processed multi-band resonant-cavity detector with the active region sandwiched between two reflectors. A Au film is used as the bottom reflector, while the top reflector can be either a native semiconductor-air interface or a dual-band DBR.

Although the DBR is not practical for the LWIR, it acts as a good reflector for the SWIR and MWIR, and is thus suitable for optimizing the top reflector. Here, a specifically designed DBR simultaneously performing as the reflector for the SWIR and MWIR is used. A dual-band DBR is shown in Figure 7 (a), with one period consisting of 378.5-nm SiO_2 , 264.8-nm TiO_2 , and 264.8-nm TiO_2 , resulting in two reflection bands centered at 1.6 μm and 3.3 μm . Figure 7 (a) shows the calculated reflection spectrum of the detector structure with a dual-band DBR at the

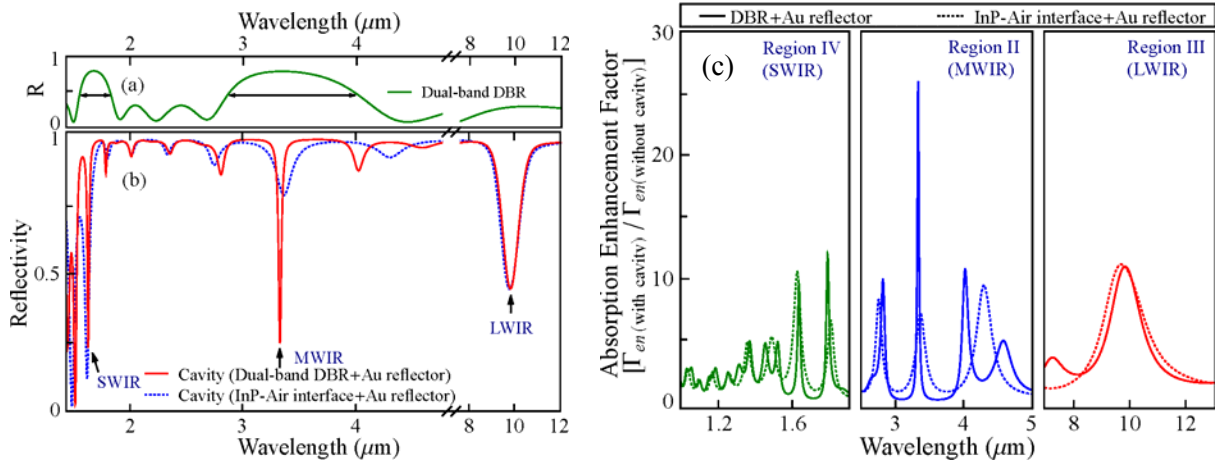


Figure 7: Calculated reflection spectra of (a) a 3-period $\text{TiO}_2/\text{SiO}_2$ dual-band DBR, and (b) whole resonant-cavity detector structures. The use of only a Au reflector (dotted line) produces resonance modes (the dips) in the whole spectral region. The solid line shows further resonance enhancement by using a SWIR-MWIR dual-band DBR without affecting the LWIR performance. Both resonance modes lie within DBR's high-reflection bands. Resonance modes for the regions of interest IV (SWIR), II (MWIR), and III (LWIR) are indicated by arrows. (c) Calculated absorption enhancement factor for the absorbing regions II, III, and IV. A factor of 11 is achieved by placing a Au reflector at the bottom side of the detectors, while the use of another top 3-period $\text{TiO}_2/\text{SiO}_2$ dual-band DBR gives rise to enhancement by a factor of 26.

top and a Au reflector at the bottom. In comparison with the one without the top DBR, dips at 1.635 and 3.325 μm are the two resonance modes being enhanced by both the DBR and Au reflectors. Enhancement factors of 12 and 26 for region IV (SWIR) and region II (MWIR) are observed. The use of dual-band DBR narrows the response peaks of both the SWIR and MWIR, which can be useful for monitoring gases by simultaneously identifying two absorbing lines. By selecting three periods of the DBR, the resonance at LWIR remains valid yielding a nearly fixed enhancement factor. This is because that the DBR is no longer a good reflector for the LWIR range, as seen in Figure 7 (a), and hence its effect only changes the cavity length for the LWIR region.

As an application, the F-P cavity optimization was applied to the already demonstrated GaAs multi-band detector⁴. The structure is similar to the one shown in Figure 6. Since the detector consists of two groups of n -type QWs, the incoming light is assumed to be TM polarized with a 45° incidence angle. The comparison of the spectral response in the cavity-enhanced multiband detectors with the experiment is shown in Figure 8. The maximum enhancement factors for MWIR and LWIR are 5.5 and 9.5, and 17 and 9 corresponding to the structure with the Au reflector alone, and both the DBR and Au reflectors, respectively. It can be seen that the use of the F-P cavity also reduces the unnecessary response outside the spectral range of interest. For example, the ratio of the peak responsivity in the 3-4 μm range to that in the 4-8 μm range is increased from 3 in the original structure without the cavity up to 9 in the cavity-enhanced detector. The expected response by cavity enhancement is promising for designing optimized multi-band detectors with higher performances as well as the desired spectral response.

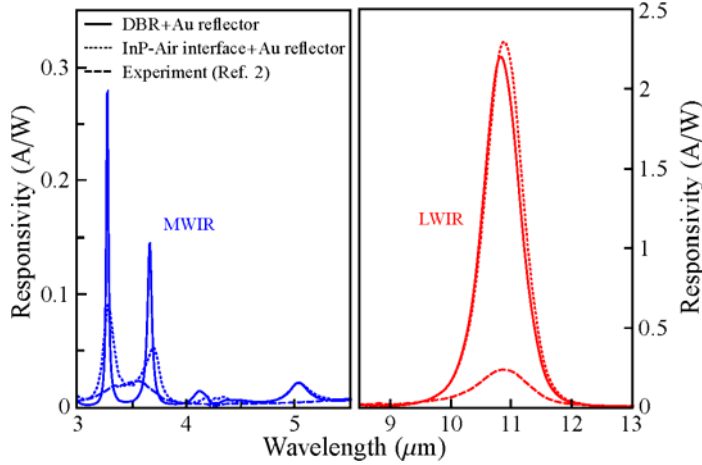


Figure 8: The optimization of the spectral response in a GaAs multi-band detector (see Ref. 7) by applying the F-P resonant cavity. The dotted and solid curves correspond to two cavity structures using a Au reflector, and both DBR and Au reflectors, respectively. The F-P resonance effects enhance the optical field and hence the QE, and also cause the splitting of the response peak between 3 - 4 μm . The DBR is designed such that enhancement only occurs in MWIR without affecting the LWIR.

3 MATERIAL CHARACTERIZATION FOR DETECTOR DESIGN

A dielectric function model for inter-valence band (IVB) transitions has been developed to evaluate the absorption. Infrared absorption of semiconductors including *p*-type GaAs and InP were measured. The absorption properties are the preliminary knowledge in order to determine the response range of the material used in split-off detectors.

3.1 Dielectric function model for *p*-type semiconductor inter-valence band transitions

The contributions of IVB transitions to the dielectric function (DF) by free holes among the split-off (SO), light-hole (LH) and heavy-hole (hh) bands have been theoretically modeled⁵ to determine the DF of two *p*-type semiconductors, GaAs and $\text{Ge}_{1-y}\text{Sn}_y$ with the Zinc-blend and Diamond crystal structures, respectively. The IVB transitions dominate the spectral range between 0.1-1eV with respect to the spin-orbit splittings between *so-hh* and *lh-hh* bands. In conjunction with inter-band transitions, free-carrier and lattice absorption, a complete DF model allows the determination of optical constants with improved accuracy in the spectral range covering both ultraviolet and infrared regions. The model should be applicable to most of the group III-V and IV materials since their valence band structures resemble the ones under investigation. Figure 6 (a) shows the model dielectric function of *p*-GaAs at different doping concentrations. Comparison of absorption between *p*-GaAs and *p*- $\text{Ge}_{1-y}\text{Sn}_y$ is shown in Fig. 6 (b) in the spectral range of 3-5 μm .

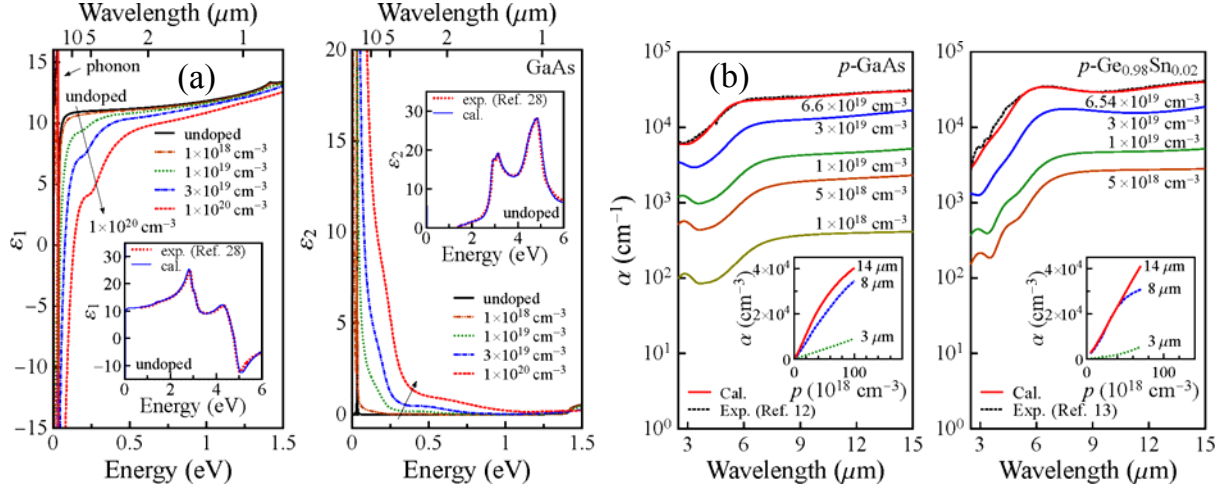


Figure 9: (a) The calculated DF (ϵ_1 and ϵ_2) for p -type GaAs at various doping concentrations. The phonon absorption induces a strong feature at the low-energy region. The FC contribution shows a $1/E^2$ behavior. The IVB transitions are responsible for the region between 0.1-1eV. The insets show the calculated DF of undoped GaAs in comparison with experimental curves. (b) Calculated absorption coefficient for p -GaAs and p -Ge_{0.98}Sn_{0.02} at different doping concentrations. The insets show the variation of absorption coefficient with the doping concentrations at 3, 8 and 14 μm .

3.2 Plasma frequency and dielectric function dependence on doping and temperature for p -type Indium Phosphide epitaxial films

The optical properties of p -type InP epitaxial films having different doping concentrations are investigated by infrared absorption measurements accompanied by reflection and transmission spectra taken from 25 – 300 K.⁶ A complete dielectric function (DF) model, including inter-valence band (IVB) transitions, free-carrier and lattice absorption, is used to determine the optical constants with improved accuracy in the spectral range from 2 – 35 μm . The reflection and transmission spectra for the doped samples are shown in Figure 10. Figure 11 (a) shows the absorption spectra. The transmission in 30 – 35 μm range is near zero; hence not shown in the figure. There is a step around 20 μm as can be seen in reflection, transmission and absorption spectra which is due to multi-phonon absorption. Even though there are many higher order phonon frequencies⁷ associated with InP material, only eight Lorentz oscillators (as shown by arrows in **Error! Reference source not found.**) were implemented to study the phonon absorption depending on their strength in absorption.

To obtain the IVB DF, parameters representing the strength (A_{ab}) and line-shape broadening (Γ_{ab}) of transitions were determined by fitting experimental data with the model output. Compared to p -GaAs,⁵ the case of p -InP is complicated by the small spin-orbit splitting ($\Delta_{so} = 110 \text{ meV}$). Therefore, SO-HH and LH-HH absorption regions are merged, unlike in p -GaAs. Because of this small Δ_{so} , much of the absorption due to direct IVB transitions occurs in a region of the IR where lattice absorption and FC absorption are strong. The insets in Figure 11 (a) show the absorption with and without IVB transitions in the 2 – 14 μm region. This shows that the difference is coming from the IVB transitions. It can also be seen that IVB absorption increases with doping. The total absorption coefficient extracted from the DF is plotted in Figure 11 (b)

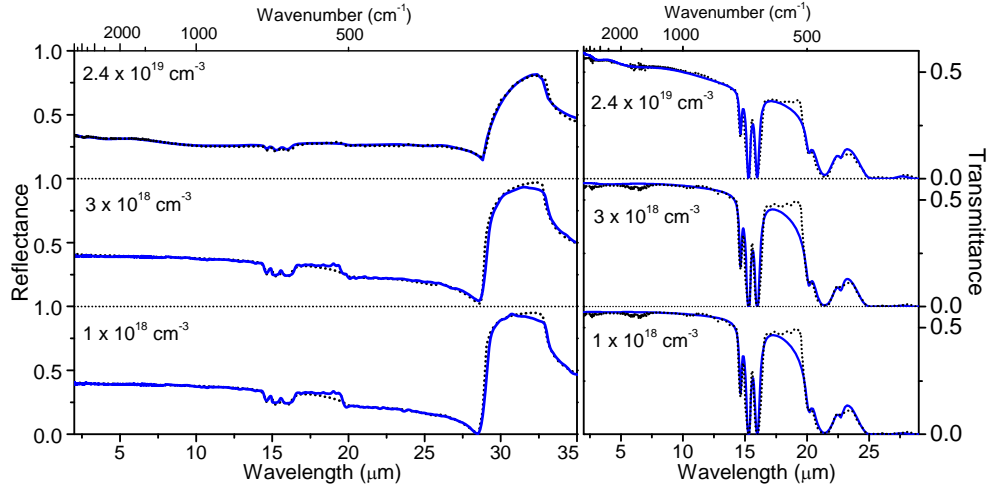


Figure 10: Experimental reflectance and transmittance spectra (dotted lines) of the sample having *p*-InP epilayers on InP substrate along with the best fit results (solid lines) at 300 K. The transmission drastically reduces beyond 20 μm and is almost zero in 30 - 35 μm range. Therefore this region for transmission is not shown. The top axis represents wavenumber (cm^{-1}) scale which is equal to $10,000/\lambda(\mu\text{m})$.

with comparisons to the experimental⁹ data for $1 \times 10^{18} \text{ cm}^{-3}$. The obtained absorption coefficient will be useful for various applications, including IR split-off band detectors designs¹.

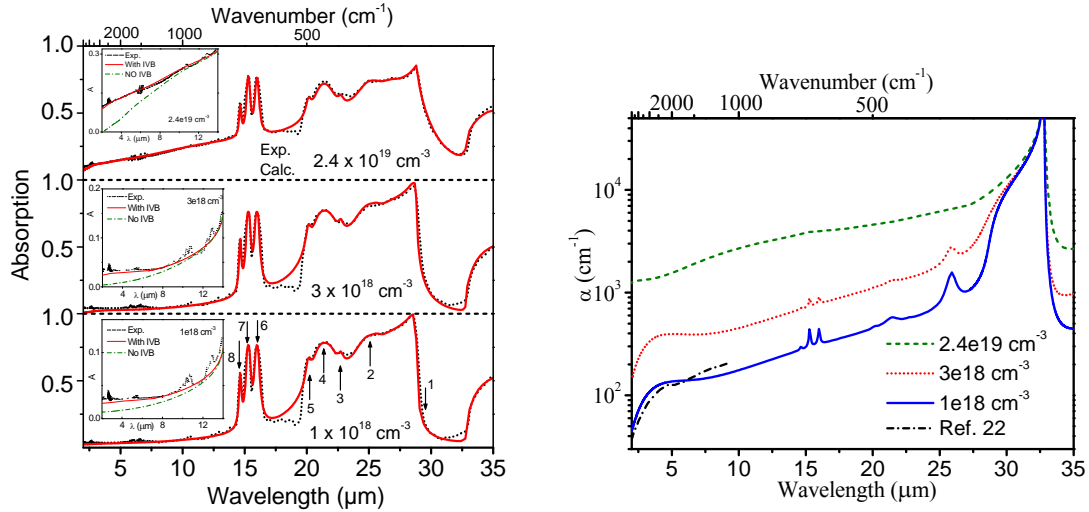


Figure 11: (a) Experimental absorption spectra (dotted lines) of the *p*-InP films on InP substrate along with their best fit results (solid lines) at 300 K. For clarity, each spectrum is successively shifted by 1 in the vertical direction. The arrows indicate the location of each Lorentzian oscillator. The insets show the enlarged region (2 – 14 μm) where IVB absorption is expected which show the absorption with and without IVB transitions. The IVB absorption increases with doping and over shadows the weaker higher order phonon peaks in 10 – 13 μm range. (b) Calculated absorption coefficient at 300 K. The strong absorption peak around 32.7 μm (306 cm^{-1}) is due to Reststrahlen absorption of the lattice structure. The weak peaks are due to the difference in phonon absorption between the doped layer and the substrate. The theoretical values are compared with the data taken from Ref.⁸ for $1 \times 10^{18} \text{ cm}^{-3}$.

One of the atmospheric windows, 8 – 14 μm is a crucial spectral region that falls into the scope of IVB effects.

3.3 Optical properties of nanostructured TiO_2 thin films and their application as antireflection coatings on infrared detectors

In semiconductor detectors, there is significant amount of reflection (up to 30% depending on the refractive index (n) of the medium and the wavelength range) from the top surface. This will reduce the light throughput to the detector and also the field of view. Use of graded-index layers for broadband antireflection (AR) properties is one of the best approaches to reduce reflection. Oblique-angle deposited titanium dioxide (TiO_2) nanorods have attracted much attention as good antireflection (AR) coating material due to their low refractive index profile.¹⁰

The obtained refractive index of TiO_2 nanorods in the infrared range from fitting to experimental transmission is shown in Figure 12. The scattered data were fitted using the Sellmeier dispersion equation. The dotted and dashed curves correspond to the Sellmeier equation obtained by least-square fitting for s - and p -polarized components (E_s and E_p), respectively.

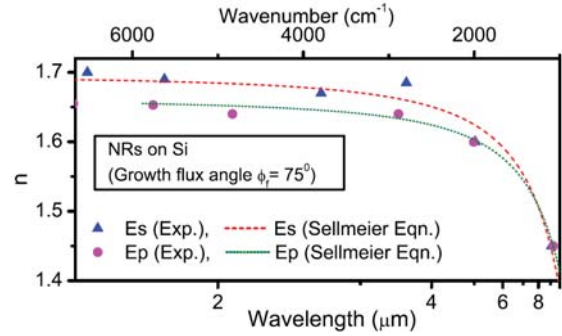


Figure 12: Refractive index obtained for a TiO_2 nanorod layer grown on Si. The dots represent the values found at FP peak positions. The dotted and dashed curves show the corresponding Sellmeier equation obtained by least-square fitting.

The obtained refractive index data are used to design AR coatings on GaN, as shown in Figure 13. The reflectance remains less than 3.3% for normal incidence for 2–8 μm spectral range and less than 10.5% even at 60° for the same spectral range.

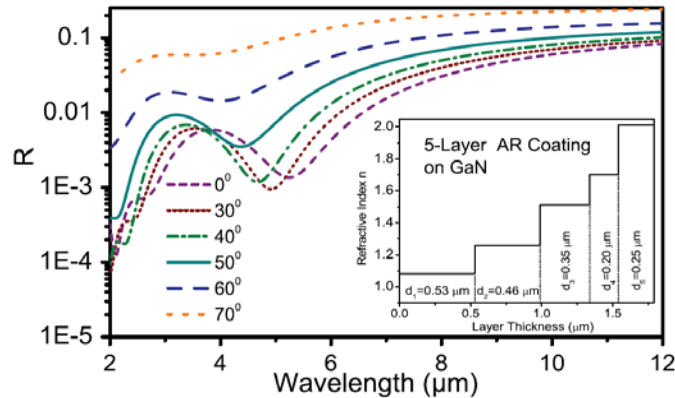


Figure 13: Reflection from five-layer AR coating structures (on GaN substrate) at oblique angles of incidence. For clarity, the curves for incident angles of 10° and 20° are not shown as they are very close to the curves for 0° . The inset shows the graded refractive index (n) profile of the AR coating from air to GaN ($n_{\text{GaN}} = 2.3$) with thickness (d_i) of each layer.

4 DEVICE RESULTS AND DISCUSSION

4.1 Effects of Graded Barriers on the Operation of Split-Off Band Infrared Detectors

Increasing the operating temperature of infrared detectors is a prime importance for practical applications. The use of split-off band transitions has been proposed for high operating temperature infrared detectors. Initial results showed increasing the potential barrier for free carrier emission has led to increases in operating temperature from 150 K for a detector with an 8 micron threshold to room temperature for detector with a 4 micron threshold. However, these detectors showed a low responsivity due to the capture of carriers in each emitter. A proposal was made to use graded barriers with an offset between the barriers on the two sides of an emitter as a method of reducing the capture in the emitters.¹¹ Two GaAs/Al_xGa_{1-x}As samples with a single graded barrier (Al fraction $x = 0.57$ to 1 and 0.45 to 0.75, respectively) were used to test the effects. The sample with the lower barrier show responsivity increased by a factor of ~ 10 or more compared to the higher graded barrier sample and detectors without the graded barrier. The higher graded barrier sample, space charge build up causes almost all potential drop across the first barrier, and hence reduces the response. Based on the modeling it is believed that this effect will be greatly reduced in detectors with multiple periods of graded barriers and emitters, allowing the full gain effects of the graded barriers to be realized.

Figure 14 (a) shows the spectral responsivity of sample 460 in which the Al fraction of the barrier is graded from 0.45 to 0.75. The barrier is lower than the split-off energy so both free carrier and split-off responses were observed. Also a very different response levels observed under forward and reverse bias. Switching the polarity of the bias leads to a three order of magnitude change in the response at 150 K. This is believed to be due to the depletion of the emitter under positive bias at this temperature. The thermally excited carriers can much more easily tunnel out of the emitter than they can enter the constant barrier over the top. This depletion leads to most of the applied field being across the constant barrier at positive bias and hence a reduced response. This effect is reduced at 80 K where the response under forward and

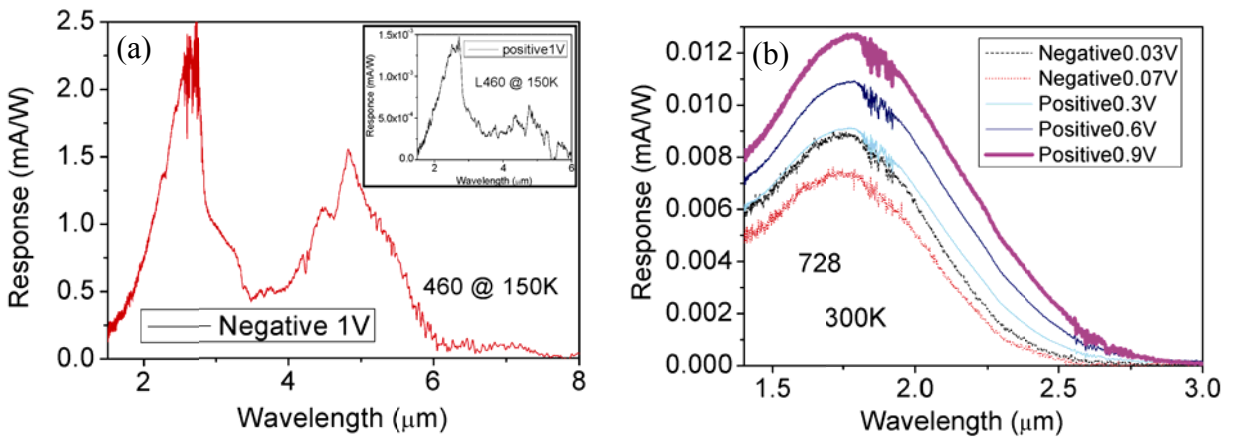


Figure 14: (a) The spectral response of 460 at 150K, showing a great difference between the forward and reverse biases. In this detector both free carrier and spitoff responses can be seen. (b) The spectral response of 728 at 300K. Only free carrier response is observed due to the barrier being above the split-off energy.

reversed bias differs by less than a factor of two. The reduction in this effect is due to the greatly reduced thermally assisted tunneling at the lower temperature. Another sample 728 has a larger potential barrier with Al fraction graded from 0.57 to 1. The spectral response is shown in Figure 14 (b). The response under negative bias is observed only at low bias values, as the safe current limit reaches it very low bias. Under these conditions, the Arrhenius data indicates the emitter is depleted, so that the response will be primarily from the bottom contact. Since the split-off energy is much less than the effective barrier height, the response is due to free-carrier absorption. For positive bias, the carriers are all trapped at the emitter.

4.2 Split-off photovoltaic infrared detection with *p*-type graded barrier heterostructures

Uncooled operation of split-off detectors with a 4 micron threshold has been previously demonstrated.¹² Further improvement on the performance of the split-off detectors was investigated by employing photovoltaic operation with zero bias applied.¹³ Operating at zero bias voltage, i.e., photovoltaic mode, will inherently suppress the dark current, leading to a reduction in the noise with an increase in the detectivity. Photovoltaic infrared detectors have significant advantages over photoconductive detectors due to zero bias operation, requiring low power and having reduced low frequency noise. They also exhibit no thermally assisted tunneling currents, leading to higher operating temperatures.

The key feature for obtaining a photovoltaic response is to have an asymmetry in the transport of photocarriers. A graded barrier connecting two *p*-type doped layers is used to achieve asymmetry as shown in Figure 15, with IVB absorption occurring in the doped emitters. The carriers escaping from the emitter and contact beside the graded barrier will then have different probabilities of passing over the barrier. The excited carriers which pass over the high barrier end, indicated as x_2 , will continue to the contact region even if they scatter in the barrier and lose energy. However, carriers excited from 'Contact 1', and move toward the emitter, will lose sufficient energy in a scattering event to be below the high end barrier x_2 , and hence will be reflected back to Contact 1. This effect will lead to a net current flow as shown in Figure 15 (b) (arrow), gradually raising the potential in Contact 1 to be higher than the emitter and Contact 2, until a built-in potential V_{ph} is established. This is the signal that is measured as a photovoltaic response of the detector.

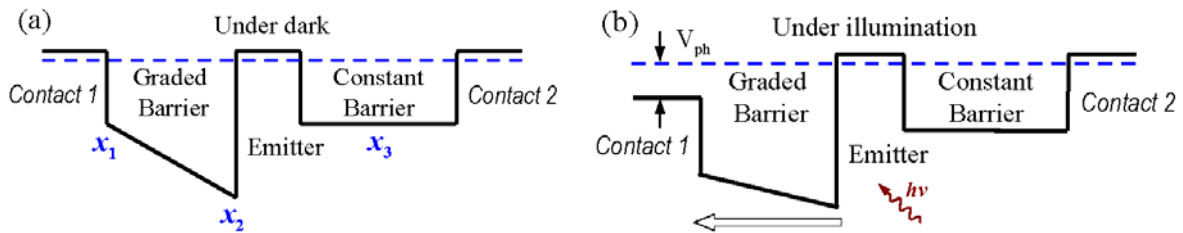


Figure 15: The valence band diagram of a single period asymmetric heterojunction structure under dark conditions. The emitter and contact layers are *p*-type doped, while barriers are undoped. (b) Under illumination, holes are excited into higher energy states with a higher probability of escaping over the emitter/barrier interface. In the presence of a graded barrier, a net flow of holes occurs, as indicated by the arrow, until a new equilibrium with a built-in potential V_{ph} is established.

In addition to photovoltaic operation, this asymmetric structure will reduce the excessive recapture of excited carriers in the emitters in previous demonstrated split-off detectors¹² without graded barriers. When the barrier on the injection side of the emitter is higher than the escape side, it will increase the energy of the carriers entering the emitter. If the difference in heights is sufficiently large, the carriers will still be able to escape after scattering and the trapping rate will be greatly reduced, this should lead to photoconductive gain. By increasing the barrier on the injection side, the dark current is reduced at low biases, because carriers need to overcome the barrier. Also by grading the higher barrier, the device will be able to operate at lower electric fields with improved sweep-out efficiency of photoexcited carriers due to low dark current.

A photovoltaic response was observed for all the tested devices with a graded barrier (V0727, V0728, SP1005, SP1006 and SP1007 as shown in Table 1) showed at room temperature. Open circuit voltage of the device was measured by a voltage amplifier (Stanford Research, SR 560) and a Perkin Elmer system 2000 FTIR. The data was calibrated using responsivity of a bolometer. Out of the tested devices, the highest signal was observed for the device from the wafer V0728, as expected through the analysis of I-V data. The open circuit voltage responsivity spectra of a device from this wafer at 280K and 300K are shown in Figure 16 (a). At 300K, a peak responsivity of 460 mV/W was observed at the wavelength of 1.8 μm and the estimated photocurrent is $\sim 40 \mu\text{A/W}$. The Johnson noise limited specific detectivity value for the device is calculated as $\sim 1.5 \times 10^6$ Jones using:

$$D^* = R_v \sqrt{\frac{A}{4kTR_0}} \quad (1)$$

Here, R_v is the responsivity in volts per watt and, R_0 is the resistance at zero bias, A is the area of the device, k is the Boltzmann constant and T is the temperature. When the temperature of the device was reduced, an increase in the responsivity and D^* to 1.28 V/W and 2.8×10^6 Jones was observed, respectively. A summary of the peak responsivity and D^* values at 300K, at 1.8 μm , are tabulated in Table 1.

Table 1: Summary of the device parameters, where X1, X2 and X3 represents the aluminum (Al) fraction of the barriers at the bottom contact and the emitter ends of the graded barrier, and at the constant barrier respectively. The responsivity and specific detectivity (D^*) of the devices at 300K, and a wavelength of 1.8 μm , are also shown.

Device No.	X1	X2	X3	Emitter thickness	Peak Responsivity (mV/W) @ 300K	D^* (Jones) @ 300 K
458	0.45	0.75	0.57	20 nm	--	--
V0727	0.55	1.0	0.57	20 nm	17.1	6.0×10^4
V0728	0.55	1.0	0.57	80 nm	450	1.2×10^6
SP1001	0.75	0.75	0.57	20 nm	--	--
SP1005	0.45	0.75	0.57	20 nm	1.1	9.9×10^3
SP1006	0.45	0.75	0.57	50 nm	3.9	3.3×10^4
SP1007	0.45	0.75	0.57	80 nm	20.8	1.4×10^5

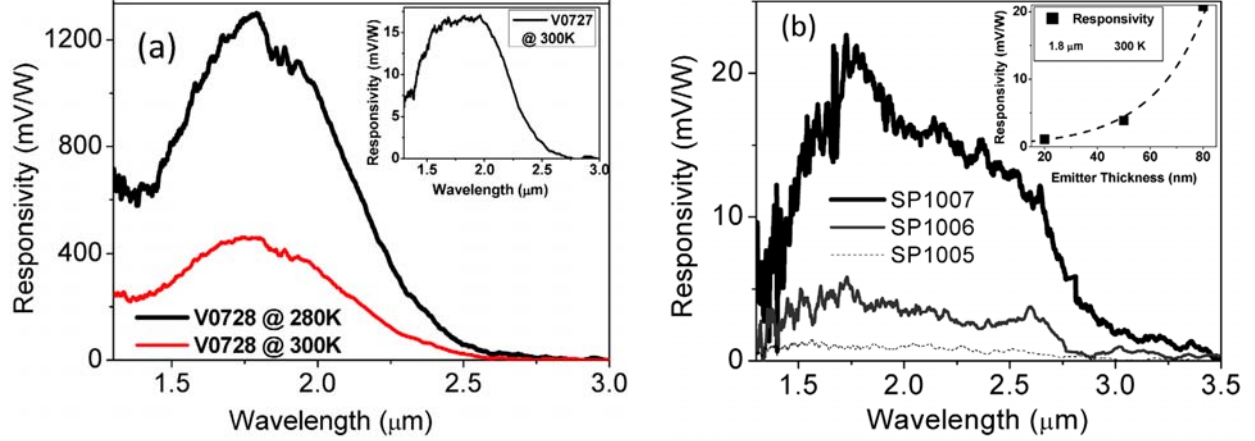


Figure 16: (a) The photovoltaic response of V0728 at 280 K and 300 K; the photovoltaic response shows a peak at a wavelength of 1.8 μm and a threshold at 2.6 μm . The photovoltaic responsivity increases with the decreasing temperature. Inset: Responsivity of wafer V0727 at 300 K. The responsivity of V0727 is lower owing to the thinner emitter, 20 nm compared to 80 nm in V0728. (b) The photovoltaic response of SP1007, SP1006 and SP1005 at 300 K. The photovoltaic response decreased with decreasing emitter thicknesses (80 nm, 50 nm & 20 nm respectively). A peak response was seen at a wavelength of 1.8 μm , and a threshold was observed at 3.5 μm . Inset: The peak responsivity (at 1.8 μm) extracted from response curves of the three devices show an exponential increase in the responsivity with increasing emitter thickness.

The responsivity spectra of SP1005, SP1006, and SP1007 at room temperature are shown in Figure 16 (b). SP1007, having a thicker emitter of 80 nm, shows a higher responsivity compared to the other two wafers (SP1006 and SP1005) which have thinner emitters of 50 nm and 20 nm, respectively. A similar behavior was observed for V0728 and V0727 (responsivity shown in inset of Figure 16 (a)); the response is higher in V0728 with an 80 nm emitter. Since each wafer has the same doping density in the emitter, the device with a thicker emitter is thus likely to have an increased charge accumulation. The higher photovoltage is a result of a higher number of carriers accumulated in the contact region. Wafer SP1001, which did not have a graded barrier, did not show a photovoltaic response when operated close to room temperatures.

The ratio of the peak responsivity (1.8 μm) for V0728 to V0727 is ~ 26 , while for SP1007 to SP1005 it is ~ 19 . This responsivity increment is much greater than the ratio in emitter thickness. The responsivity increase in the SP devices with emitter thickness is shown in the inset of Figure 16 (b), and is showing an exponential behavior. The difference in the responsivity ratios between V07 and SP wafers may, however, be a result of the difference in the aluminum fractions in the graded barriers (the gradient in the barrier). Additionally due to the differences in the device resistance, the accumulated carriers may discharge quickly in the SP series devices compared to the V07 series.

The variation in D^* for V0728 with wavelength in the photoconductive mode (with a bias of -0.1 V) and photovoltaic mode (0 V bias) are shown in the

Figure 17. The noise generated by the measuring instruments is negligible compared to the device noise. The inset of

Figure 17 shows the noise current density ($S(f)$) of V0728 at a -0.1 V bias voltage, and at 0 V bias. At high frequency ($f > 10$ kHz) the measured noise density is closer to the Johnson noise

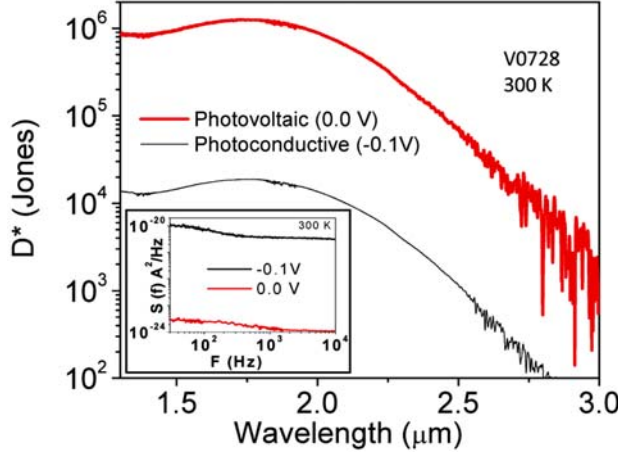


Figure 17: Detectivity of V0728 as a function of wavelength in a photoconductive mode (with a bias of -0.1V) and photovoltaic mode (0 V bias) at 300 K. Photovoltaic mode have a higher detectivity due to low noise. Inset: The noise current density ($S(f)$) of V0728 at -0.1V bias voltage, and 0 V bias, shows a low noise level in the device with 0V bias due to absence of shot noise caused by dark current in biased device.

limit. D^* calculated with the measured noise at 10 kHz, is 1.2×10^6 Jones. As a comparison between the

photovoltaic and photoconductive modes of operation, sample V0728 was then operated in photoconductive mode

under the negative bias (bottom contact positive) for which it was designed. The D^* value of 1.5×10^6 Jones for photovoltaic operation was significantly higher than the photoconductive value of 3.5×10^4 Jones. This indicates the potential for better performances of devices, in the photovoltaic mode of operation using graded barriers at room temperature.

4.3 Light-hole and heavy-hole transitions for high-temperature long-wavelength infrared detection

Hole transitions from the heavy-hole (hh) to the light-hole (lh) band contributing to the 4-10 μm response range are reported on p -GaAs/ AlGaAs detectors.¹⁴ The detectors show a spectral response up to 16.5 μm , operating up to a temperature of 330 K where the $lh-hh$ response is superimposed on the free-carrier response. Two characteristic peaks observed between 5-7 μm are in good agreement with corresponding energy separations of the lh and hh bands and thus originated from $lh-hh$ transitions. Figure 16 shows the spectral response of different detectors. The comparison of experimental response with theoretical calculation with free-carrier absorption contribution alone (dashed line) indicates that the $lh-hh$ transitions have a primary contribution to the 4-8 μm response range. Different features than optical absorption are the response peaks at 5.50 μm and 6.46 μm . Their corresponding energy values (0.225 eV and 0.192 eV, respectively) are in agreement with reported $lh-hh$ separations along the Λ (111) and Δ (001) directions. Room-temperature response up to 330 K was observed in long-wavelength range between 4-16.5 μm . Results will be useful for designing multi-spectral detection which could be realized on a single p -GaAs structure.

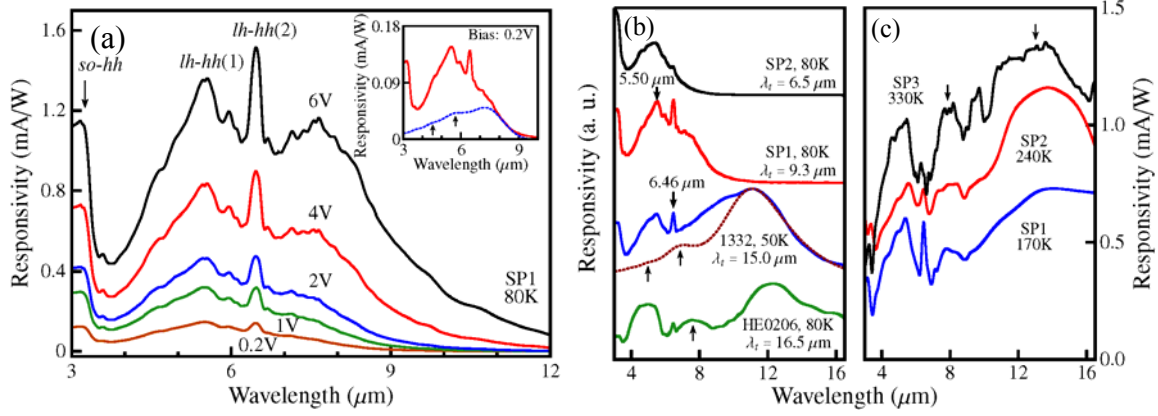


Figure 18: (a) The 80 K responsivity spectra of SP1 at different bias. The inset shows a comparison with modeled responsivity (dashed line) at 0.2 V bias with FCA contribution alone. Peaks indicated by arrows are interference modes of the p-GaAs/AlGaAs periodic layers. (b) Spectral response of detectors with varied threshold wavelengths (λ_t). The curves from top to bottom are measured at the bias of 8 V, 2 V, 1 V, and 2 V, respectively. In comparison with the FCA response (dashed line) calculated for the detector 1332, *lh-hh* transitions produce response between 4–10 μm . (c) High-operating-temperature capability was measured on samples SP1, SP2, and SP3 under 0.2 V, 0.3 V, and 3 V, respectively, showing broad range from 4–16.5 μm . The wavelength region above designed threshold is due to a thermal detection mechanism. Cavity interference modes are all marked with the arrows in (a) and (b).

4.4 ZnO-Based UltravioletInfrared Dual-Band Detector Sensitized With PbS Quantum Dots

A low-cost photoconductive dual band detector based on lead sulfide quantum dots (PbS-QDs) sensitized nonporous ZnO film is manufactured on the surface of the fluorine doped tin oxide (FTO) conducting glass plate.¹⁵ Figure 19 shows the spectral responsivity. The ultraviolet (UV) response arises as a result of interband absorption of UV radiation by ZnO and infrared (IR) response

is due to the absorption in PbS-QDs. The detector exhibits UV response from 200 - 400 nm with a peak responsivity of 4.0×10^5 V/W and detectivity (D^*) of 5.5×10^{11} Jones at 370 nm under room temperature. Observed visible-near IR response is from 500 - 1400 nm with a responsivity of 5.4×10^5 V/W and D^* of 7.3×10^{11} Jones at 700 nm operating at room temperature. By increasing the PbS-QD size, IR response can be extending up to 2.9 μm .

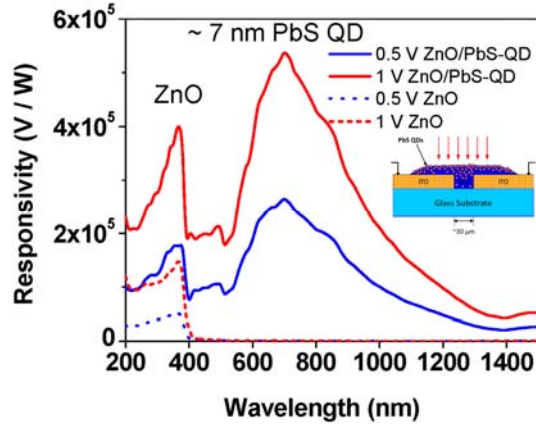


Figure 19: Spectral responsivity of the dual-band detector compared with the ZnO detector without PbS QDs. Inset: the schematic of dual-band PbS-QD embedded colloidal ZnO detector.

4.5 Surface Plasmon for Optimizing Detector Performance Heterojunction plasmonic midinfrared detectors

Metal corrugated surfaces have the potential of enhancing optical absorption through surface plasmon (SP) excitation facilitated by light-metal interactions. We have carried out designs with Plasmon enhancements in the conventional heterojunction mid-infrared detectors, optimized for their operation in 8-14 μm spectral range.¹⁶⁻¹⁷ Design issues concerning GaAs-AlGaAs based plasmonic photodetectors are investigated using modal expansion method (MEM) in conjunction with Rayleigh expansion. Simple but insightful fitting expressions useful for designing practical photodetectors are presented. The effects of crucial design parameters on the photodetector performance are discussed in detail. Using metallic grating based plasmonic element, about 20 fold absorption enhancement is predicted, which is comparable or greater than that recently reported for InAs (Quantum Dots) and GaInNAs (Quantum Well) detectors.

A schematic of the representative structure is shown in Figure 20 (a). Absorption spectra for grating period ($\Lambda = 3.2 \mu\text{m}$) are also shown. The main features of these spectra are: (i) appearance of resonant absorption peaks spanning mid-infrared spectral window, (ii) blue-shift of resonant wavelength λ_p with increasing metallic height h_1 till λ_p becomes independent of further increase at a characteristic wavelength, (iii) red-shift of resonant wavelength λ_p with increasing grating period, (iv) substantial absorption enhancement in the presence of plasmonic element relative to the bare structure, and (v) increased peak asymmetry toward shorter wavelengths. The quantitative estimation of absorption enhancement as a function of emitter thickness for three different wavelengths (10, 11, and 12 μm) is shown in Figure 20 (b).

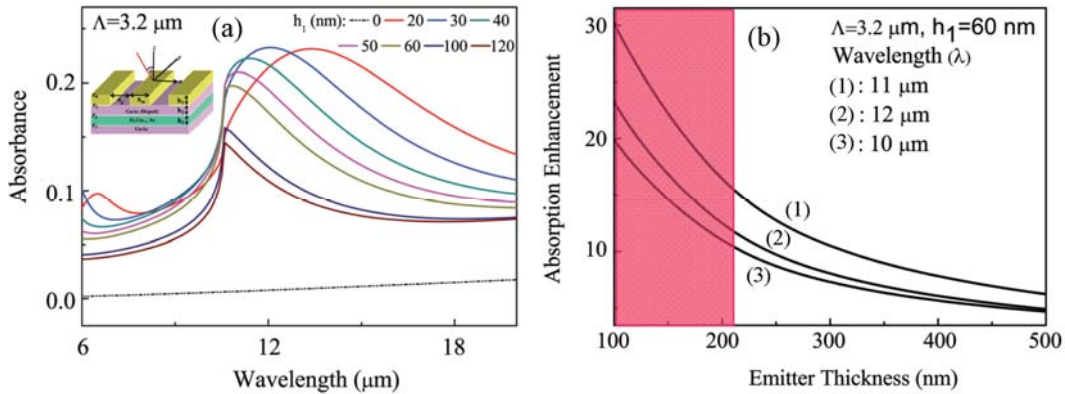


Figure 20: (a) The calculated absorption spectrum for the metallic corrugation structure shown in the inset with the period $\Lambda = 3.2 \mu\text{m}$ and different heights. The absorption for the structure without grating is also shown (dotted curve). (b) Estimated absorption enhancement as a function of (doped) GaAs emitter thickness. Plots for three excitation wavelengths (1) 11 μm , (2) 12 μm , and (3) 10 μm are shown. For practical emitter thickness range absorption is significantly increased which is about 20 fold relative to the noplasmic counterpart.

4.6 Highly sensitive GaAs/AlGaAs heterojunction bolometer

GaAs/AlGaAs multilayer heterojunction structures with different Aluminum (Al) fractions and emitter doping densities have been tested to identify optimum parameters for high temperature coefficients of resistance (TCR).¹⁸ Figure 21 (a) plots the variation of TCR in multilayer

heterojunction structures with different p-type doping densities compared to a structure with n-type doping, indicating higher TCR of p-doped structures. The inset shows the increase of TCR variation with the Al fraction x in the barrier layer of p-GaAs/ $\text{Al}_x\text{Ga}_{1-x}\text{As}$ structures SP001, SP002 and SP003 ($x = 0.28, 0.37, 0.57$, respectively). This TCR is higher than that of VO_x or α -Si bolometers. At low temperatures (50 K) some of these devices have shown TCR values of over 30%. Moreover, SP003 showed a TCR value around $4\% \text{ K}^{-1}$ at room temperature.

The specially mounted sample has the same structure as SP003. The measured response spectrum of the specially mounted sample is given in Figure 21 (b). It shows a wavelength independent (at) response up to $20 \mu\text{m}$ as expected for a bolometer. With a 2.25 V bias across the top and bottom contacts, the device shows a detectivity (D^*) of 1.7×10^6 Jones, with a responsivity of 3.7 mA/W at $10 \mu\text{m}$, operating at room temperature. The response peaks appearing in the range $2\text{--}6 \mu\text{m}$ are due to inter-valence-band transitions. fraction (SP003) shows the highest TCR value of $8.1 \pm 0.4\% \text{ K}^{-1}$ at 140 K. Additionally, the SP003 sample also shows a TCR of $\sim 4 \pm 0.5\% \text{ K}^{-1}$ at around room temperature. This value is 2 times of the TCR value of VO_x bolometers ($\sim 2\% \text{ K}^{-1}$).

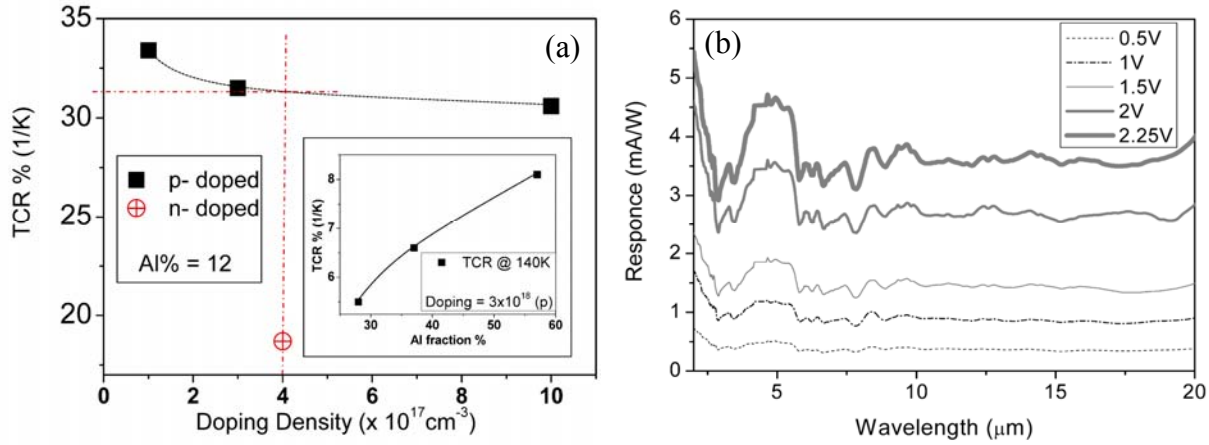


Figure 21: (a) Variation of TCR with doping density of a multilayer heterojunction structure. The structure consists with 12 layers of GaAs/AlGaAs emitter barrier regions (square for p-type and circle for n-type). TCR values are calculated at the temperature 50K with 1V bias across the structure. The dotted lines (horizontal & vertical) show the intercept point of the TCR interpolated curve for a $4 \times 10^{17} \text{ cm}^{-3}$ p-doped structure. Inset: Variation of TCR with Al fraction of a multilayer heterojunction structure. The structure consists of 30 layers of GaAs/AlGaAs emitter/barrier regions with $3 \times 10^{18} \text{ cm}^{-3}$ p-doped emitter regions. TCR values are calculated at the temperature 140K with 1V bias across the structure. (b) Responsivity of the sample consisting of 30 layers of GaAs/AlGaAs junctions with $3 \times 10^{18} \text{ cm}^{-3}$ p-doped GaAs regions and Al fraction of 57% (SP003), at different bias voltages.

4.7 High-performance, long-wave ($\sim 10.2 \mu\text{m}$) InGaAs/GaAs quantum dot infrared photodetector with quaternary $\text{In}_{0.21}\text{Al}_{0.21}\text{Ga}_{0.58}\text{As}$ capping

A high-performance InGaAs/GaAs vertical quantum dot infrared photodetector (QDIP) with combined barrier of quaternary $\text{In}_{0.21}\text{Al}_{0.21}\text{Ga}_{0.58}\text{As}$ and GaAs was investigated.¹⁹ To obtain a QDIP with a dark current level that is as small as possible to enhance detectivity, uncoupled

InGaAs/GaAs QDs were capped with a relatively thick combination barrier comprising a 30-Å layer of quaternary $\text{In}_{0.21}\text{Al}_{0.21}\text{Ga}_{0.58}\text{As}$ and a 500-Å layer of GaAs. This thick barrier is incorporated in the QD heterostructure in order to check carrier tunneling in adjacent dot layers at high temperature and a concurrent lowering of the dark current level. It has been reported that by increasing the thickness of the active region with appropriate spacer layers, the thermionic emission and tunneling contributions to the dark current can be reduced. In the present study, the heterostructure was grown by using molecular beam epitaxy (MBE) technology in the n-i(QD)-n configuration on a semi-insulating $\langle 001 \rangle$ GaAs substrate. Both the QD layer and the combination capping were repeated 35 times (Figure 22 (a) inset).

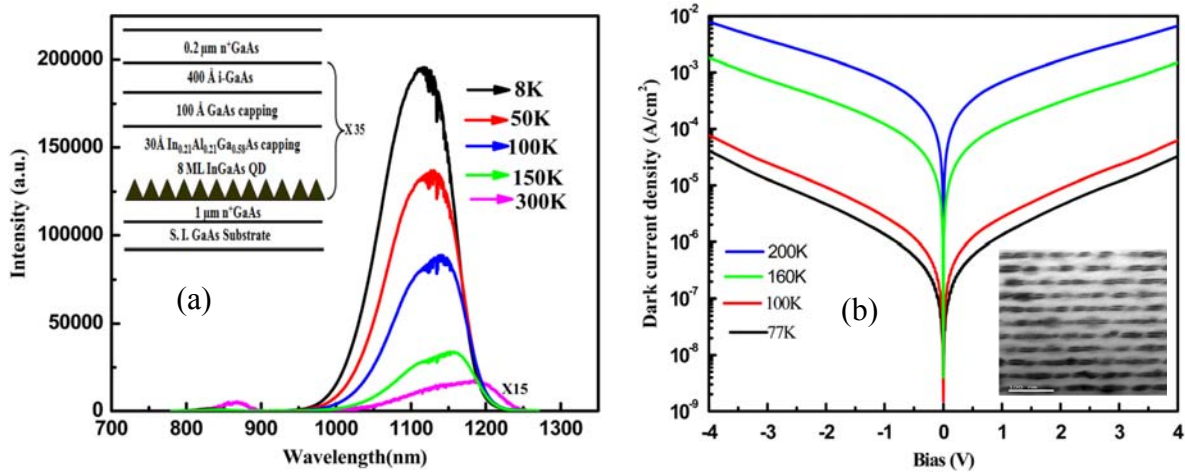


Figure 22: Calculated reflection spectra of (a) a 3-period $\text{TiO}_2/\text{SiO}_2$ dual-band DBR, and (b) whole resonant-cavity detector structures. The use of only a Au reflector (dotted line) produces resonance modes (the dips) in the whole spectral region. The solid line shows further resonance enhancement by using a SWIR-MWIR dual-band DBR without affecting the LWIR performance. Both resonance modes lie within DBR's high-reflection bands. Resonance modes for the regions of interest IV (SWIR), II (MWIR), and III (LWIR) are indicated by arrows. (c) Calculated absorption enhancement factor for the absorbing regions II, III, and IV. A factor of 11 is achieved by placing a Au reflector at the bottom side of the detectors, while the use of another top 3-period $\text{TiO}_2/\text{SiO}_2$ dual-band DBR gives rise to enhancement by a factor of 26.

The technological significance of using an InAlGaAs cap in these structures is that it acts as a surface strain-driven phase-separation alloy that is activated by surface-strain modulation across the InAs QD layer. As the QDs are covered by the quaternary cap, the In adatoms from the alloy migrate toward the relaxed dots, resulting in a compositional In gradient across the periphery of the islands. This gradient prevents intermixing of the QDs and the barrier material during MBE growth, thereby preserving the shape of the QDs. Overall strain in the structures restricts the possible number of dot layers in a multilayer structure; hence, combination capping was chosen. In such capping, the subsequent overgrowth of the quaternary alloy with a high temperature grown GaAs layer helps to planarize the growth front for the next QD layer due to increased Ga mobility at elevated temperatures. Note that quaternary cap composition is chosen so that it is perfectly lattice-matched with the GaAs, according to Vegard's law and has a similar band-gap energy. Thus, a drawback of the dot-in-a-well approach is avoided with the structure.

The QD profile of our heterostructure was confirmed by using cross-sectional transmission electron microscopy (XTEM) as shown in the inset of Figure 22 (b). There was no evidence of defects or dislocations in the heterostructure. The absence of defects helps to enhance responsivity. To determine the optical quality of the material, temperature-dependent photoluminescence (PL) measurement was performed and shown in Figure 22 (a). An intense PL peak from the sample is observed in the $1.12\ \mu\text{m}$ range at 8K. The persistence of PL emission from the sample until $\sim 150\text{K}$ indicates the low density of defects in the heterostructure. The full width half maximum (FWHM) of the emission peak at 150K is $\sim 40\ \text{nm}$. A room temperature (300 K) emission peak from the heterostructure is also shown in Figure 22 (a).

To test QDIP performance, $0.4 \times 0.4\text{mm}$ detector test mesas were fabricated. The device's dark current density as a function of bias is shown in Figure 22 (b). The symmetry in the current-voltage curve, for both positive and negative bias, indicates the uniformities in the structural parameters of the QDs. The symmetry in the dark current characteristic also indicates that the effect of the asymmetric position of the InAlGaAs barrier in the device structure is minimal, confirming our claim that the specific composition of the quaternary alloy has a similar band-gap energy as that of GaAs. Current tunneling has been minimized in our heterostructures by the use of uncoupled QDs with a thick combination cap. Hence, the dark current density is significantly low ($1.36 \times 10^{-6}\ \text{A}/\text{cm}^2$ at 77K and $6.92 \times 10^{-4}\ \text{A}/\text{cm}^2$ at 200K, both at 1 V) in our heterostructures.

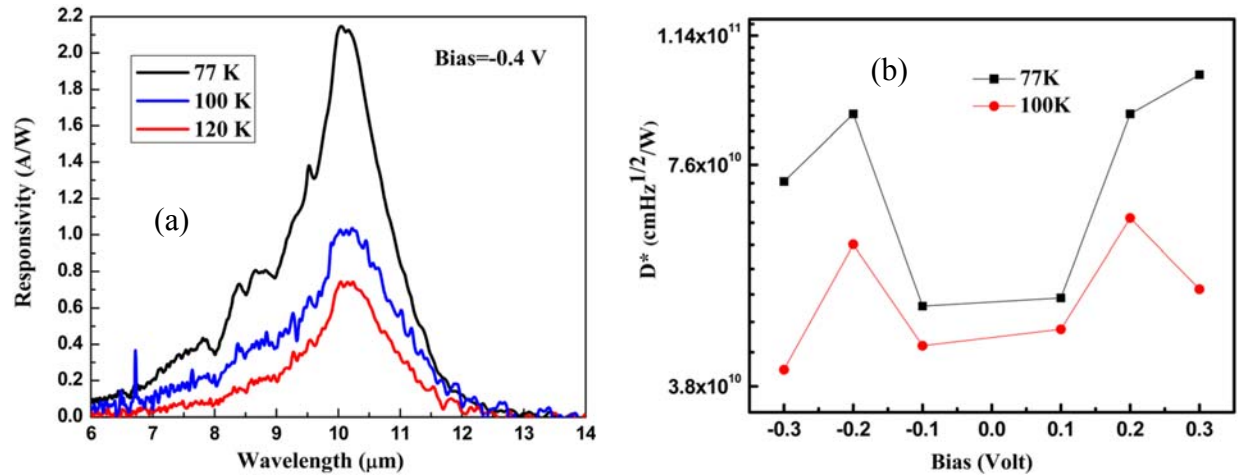


Figure 23: Calculated reflection spectra of (a) a 3-period $\text{TiO}_2/\text{SiO}_2$ dual-band DBR, and (b) whole resonant-cavity detector structures. The use of only a Au reflector (dotted line) produces resonance modes (the dips) in the whole spectral region. The solid line shows further resonance enhancement by using a SWIR-MWIR dual-band DBR without affecting the LWIR performance. Both resonance modes lie within DBR's high-reflection bands. Resonance modes for the regions of interest IV (SWIR), II (MWIR), and III (LWIR) are indicated by arrows. (c) Calculated absorption enhancement factor for the absorbing regions II, III, and IV. A factor of 11 is achieved by placing a Au reflector at the bottom side of the detectors, while the use of another top 3-period $\text{TiO}_2/\text{SiO}_2$ dual-band DBR gives rise to enhancement by a factor of 26.

The spectral responses are shown in Figure 23 (a) at different temperatures. The high-intensity response observed at $10.2\ \mu\text{m}$ is probably due to the bound-to-bound transition of carriers in the QDs. The narrow spectral width clarifies bound-to-bound transition within the QDs. The responsivity decreasing with increasing temperature is because the excited states become more populated. It can also be attributed to the short carrier lifetimes at high temperatures. The highest

specific detectivity (D^*) value for the QDIP structure is 1.01×10^{11} cm Hz^{1/2}/W at 77K at a 0.3V bias. Figure 23 (b) also shows that the 100K detectivity of the device at a 0.20V bias is quite high (6.4×10^{10} cm Hz^{1/2}/W), indicating the significance of the device structure for operation at high temperatures. Low detectivity values in QDIPs are mainly due to the high dark current, which in our heterostructure is alleviated by introducing a thick barrier layer.

References:

1. S. G. Matsik, P. V. V. Jayaweera, R. C. Jayasinghe, A. G. U. Perera, K. K. Choi and P. Wijewarnasuriya, J. Appl. Phys. **106**, 1064503 (2009).
2. Y. F. Lao, P. V. V. Jayaweera, S. G. Matsik, A. G. U. Perera, H. C. Liu, M. Buchanan and Z. R. Wasilewski, Electron Devices, IEEE Transactions on **57** (6), 1230-1236 (2010).
3. Y.-F. Lao, G. Ariyawansa and A. G. U. Perera, J. Appl. Phys. **110** (4), 043112-043117 (2011).
4. G. Ariyawansa, Y. Aytac, A. G. U. Perera, S. G. Matsik, M. Buchanan, Z. R. Wasilewski and H. C. Liu, Appl. Phys. Lett. **97** (23), 231102-231103 (2010).
5. Y.-F. Lao and A. G. U. Perera, J. Appl. Phys. **109** (10), 103528-103529 (2011).
6. R. C. Jayasinghe, Y. F. Lao, A. G. U. Perera, M. Hammar, C. F. Cao and H. Z. Wu, J. Phys.: Condens. Matter **24** (43), 435803 (2012).
7. E. S. Koteles and W. R. Datars, Solid State Commun. **19**, 221-225 (1976).
8. C. H. Henry, R. A. Logan, F. R. Merritt and J. P. Luongo, IEEE J. Quantum Electron. **19** (6), 947 (1983).
9. C. Henry, R. Logan, F. Merritt and J. Luongo, Quantum Electronics, IEEE Journal of **19** (6), 947-952 (1983).
10. R. C. Jayasinghe, A. G. U. Perera, H. Zhu and Y. Zhao, Opt. Lett. **37** (20), 4302-4304 (2012).
11. A. G. U. Perera, S. G. Matsik, D. P. Pitigala, Y. F. Lao, S. P. Khanna, L. H. Li, E. H. Linfield, Z. R. Wasilewski, M. Buchanan, X. H. Wu and H. C. Liu, Infrared Physics & Technology **54** (3), 296-301 (2011).
12. P. V. V. Jayaweera, S. G. Matsik, A. G. U. Perera, H. C. Liu, M. Buchanan and Z. R. Wasilewski, Appl. Phys. Lett. **93** (2), 021105-021103 (2008).
13. P. K. D. D. P. Pitigala, S. G. Matsik, A. G. U. Perera, S. P. Khanna, L. H. Li, E. H. Linfield, Z. R. Wasilewski, M. Buchanan and H. C. Liu, J. Appl. Phys. **111** (8), 084505 (2012).
14. Y. F. Lao, P. K. D. D. P. Pitigala, A. G. U. Perera, H. C. Liu, M. Buchanan, Z. R. Wasilewski, K. K. Choi and P. Wijewarnasuriya, Appl. Phys. Lett. **97** (9), 091104-091103 (2010).
15. P. V. V. Jayaweera, P. K. D. D. P. Pitigala, S. Jia Feng, K. Tennakone, A. G. U. Perera, P. M. Jayaweera and J. Baltrusaitis, IEEE Trans. Electron Devices **57** (10), 2756-2760 (2010).

16. M. S. Shishodia, P. V. V. Jayaweera, S. G. Matsik, A. G. U. Perera, H. C. Liu and M. Buchanan, *Photonics and Nanostructures - Fundamentals and Applications* **9** (1), 95-100 (2011).
17. M. S. Shishodia and A. G. U. Perera, *J. Appl. Phys.* **109** (4), 043108-043109 (2011).
18. P. K. D. D. P. Pitigala, P. V. V. Jayaweera, S. G. Matsik, A. G. U. Perera and H. C. Liu, *Sensors and Actuators A: Physical* **167** (2), 245-248 (2011).
19. S. Chakrabarti, S. Adhikary, N. Halder, Y. Aytac and A. G. U. Perera, *Appl. Phys. Lett.* **99** (18), 181102 (2011).